Early Stages of Agglomeration and Deposition of Adhesive Micron-sized Particles in Fully-Developed Turbulent Pipe Flows

J. Hærvig[a,*], K. Sørensen[a], T.J. Condra[a]

[a] *Aalborg University, Department of Energy Technology, Pontoppidanstræde 111, DK-9220 Aalborg, Denmark*

Abstract

This study presents numerical results on how micron-sized adhesive particles agglomerate and deposit in fully-developed turbulent pipe flows. Particle-particle and particle-wall interactions are modelled using the mechanistically-based soft-sphere Discrete Element Method (DEM) and fluid turbulence is resolved using Large Eddy Simulations (LES). In this study, the adhesive behaviour of particles, ultimately resulting in agglomeration and deposition of particles, is predicted using JKR theory.

In this study, the agglomerating behaviour of mono-sized particles with constant volume fraction $\phi = 0.001$ in turbulent flows with $\mathrm{Re} = U \cdot D/\nu = 10,000$ is investigated. By varying the Stokes number $\mathrm{St} = \rho_\mathrm{p} d_\mathrm{p}^2 U/(18\mu D)$ in the range 0.4 to 25.6, the study presents results on how changes in dominant collision mechanism affect the agglomeration rate. The results show highest agglomeration rate for intermediate Stokes numbers where the accelerative-correlated collision mechanism is dominant. At either extreme of lower or higher Stokes number, the agglomeration rate is decreased. Furthermore, at low Stokes numbers, the radial particle concentration is almost uniform throughout the flow field. At higher Stokes numbers, particles tend to accumulate either accumulate in the centre of the pipe or deposit on the wall.

Furthermore, to investigate the transition from weakly adhesive particles to highly adhesive particles, the non-dimensional adhesiveness parameter $\mathrm{Ad} = \gamma/(\rho_\mathrm{p} U^2 d_\mathrm{p})$ is varied at constant elasticity parameter $\lambda = E/(\rho_\mathrm{p} U^2)$ and

*Corresponding author. Tel.: +45 22 50 81 31
Email address: jah@et.aau.dk (J. Hærvig)

coefficient of restitution e. The results show a sharp increase in agglomeration rate and fraction of particles captured by the wall.

Keywords: Adhesive particles, Agglomeration, Deposition, Turbulent pipe flow, Large Eddy Simulation (LES), Discrete Element Method (DEM), Johnson-Kendall-Roberts (JKR)

1. Introduction

The transport, agglomeration and subsequently deposition of small adhesive particles play important roles in many industrial and fundamental processes. These processes range from particles accumulating at heat transfer surfaces, particles blocking pores in membrane filtration systems, particles being inhaled and deposited in our lungs to interstellar medium agglomerating causing early stages of new planets to form in space.

All agglomeration and deposition processes are a result of particles colliding with one another or a wall. The mechanisms governing particle collisions of non-adhesive particles in turbulent flows have been devoted much attention in literature. These studies date back to Saffman and Turner [1] who investigated the collision frequency in isotropic turbulent flows in the limiting case of finite size tracer particles with response times much than fluid response time $\tau_\mathrm{p} \ll \tau_\mathrm{f}$ and Abrahamson [2] who investigated the collision frequency in the other limiting case of heavy particles with $\tau_\mathrm{p} \gg \tau_\mathrm{f}$. For particles having $\tau_\mathrm{p} \approx \tau_\mathrm{f}$, various correlations have been proposed in literate [3]. However, as particles begin to adhere and the turbulent flow of interest is anisotropic, e.g. a pipe flow, a common approach is to resolve only the turbulence scales that affect motion of the particles considered using LES.

Different approaches exist to model the agglomeration process. One approach is to represent agglomerates by equivalent spheres that grow in size as the number of particles contained in the agglomerate increase [4, 5]. However, as shown by Brasil et al. [6], the morphology of agglomerates differs significantly depending on how the agglomerates are formed, the properties

of the primary particles and properties of the fluid flow surrounding the particles. Based on the Euler-Lagrangian approach, Sommerfeld and Stübing [7] proposed a computational efficient agglomerate structure model. Using this model, agglomerates are treated as point particles that carry additional information such as locations of the primary particles and binding forces holding the agglomerates together. Based on these properties, parameters such as the convex hull and fractal dimension can be calculated and used to relate agglomerate structure to flow resistance coefficients.

Another approach is to track each particle but assume the particles to stay adhered when agglomerated or deposited on a wall. However, the DEM study of laminar channel flow by Marshall [8] shows that phenomena such as bending and break-off of agglomerates occur frequently and play important roles to accurately predict the state where the rate of particles being re-entrained back into the fluid asymptotically approaches the rate of particles being deposited. Furthermore, the study suggests the mechanism of agglomerates continuously breaking up as agglomerates are formed to be controlled by impacting particles or agglomerates rather that fluid forces.

As noted in most studies coupling DEM to a fluid phase, there is typically a large difference between the time step sizes required to resolve particle collisions δt_{DEM} and fluid flows δt_{f}, so that $\delta t_{\mathrm{col}} \ll \delta t_{\mathrm{f}}$. As $\delta t_{\mathrm{col}} = \mathcal{O}(10^{-9}\ \mathrm{s})$, this is also valid for a wide range of turbulent flows. This fact is commonly used to speed up coupled simulations by introducing softer particles by lowering the particle stiffness and thereby making particle collisions take place over longer time periods. However, as noted in studies by Kobayashi et al. [9], Gu et al. [10], Hærvig et al. [11], depending on the adhesiveness model, introducing softer particles should be accompanied by a lower adhesive forces in order for the collision outcome (stick/rebound) to stay the same.

When the agglomerates increase in size, the study by Dizaji and Marshall [12] shows that the local fluid velocity in an agglomerate becomes increasingly correlated with the agglomerate velocity. In this case, a two-way coupling between particles and fluid is needed to accurately represent the presence

of particles on the fluid. Furthermore, due to differences in agglomerate morphology, it is not trivial to model the particle-fluid interaction without resolving the flow fluid around each particle. Attempts to correlate particle drag with particle volume fraction and Reynolds number include Ergun and Orning [13] who experimentally correlated pressure gradients in fluidized beds to the particle void fraction. Later studies by Hill et al. [14, 15] rely on the Lattice-Boltzmann Method (LBM) to resolve the flow around particles and correlate the drag force exerted on particles with particle volume fraction and the Reynolds number. While this method is highly accurate for homogeneous packing, the spatial variations in agglomerates that range from compact to dendritic in structure complicate the formulation of a general drag model. Dietzel and Sommerfeld [16] resolved the flow in agglomerates by local grid-refined Lattice-Boltzmann Method (LBM) simulations and correlated the overall drag force on different agglomerate morphologies to the projected cross section of the convex hull perpendicular to the mean flow direction. However, as the agglomerating and break-up mechanisms are governed by the particles being affected by different fluid forces, this approach is not suitable for this study.

While numerous studies on two-way coupled particle-fluid interactions have been reported, only a few account for the adhesive behaviour by fully resolving collision using the soft-sphere DEM approach. Afkhami et al. [17] studied the effect of particle adhesiveness using three different particle surface energy densities and showed a direct link between surface energy density and agglomeration rate.

The purpose of this study is look into how particle response time and particle adhesiveness affect the agglomeration rate. To obtain a fully-developed flow, the computational domain is made periodic in the stream-wise direction. To avoid imposing any limitations on the agglomeration process, the soft-sphere DEM approach is used to resolve how particles collide, agglomerate, deposit and are re-entrained into the fluid due to collisions with other particles or by fluid forces. Figure 1 gives an overview of these different processes.

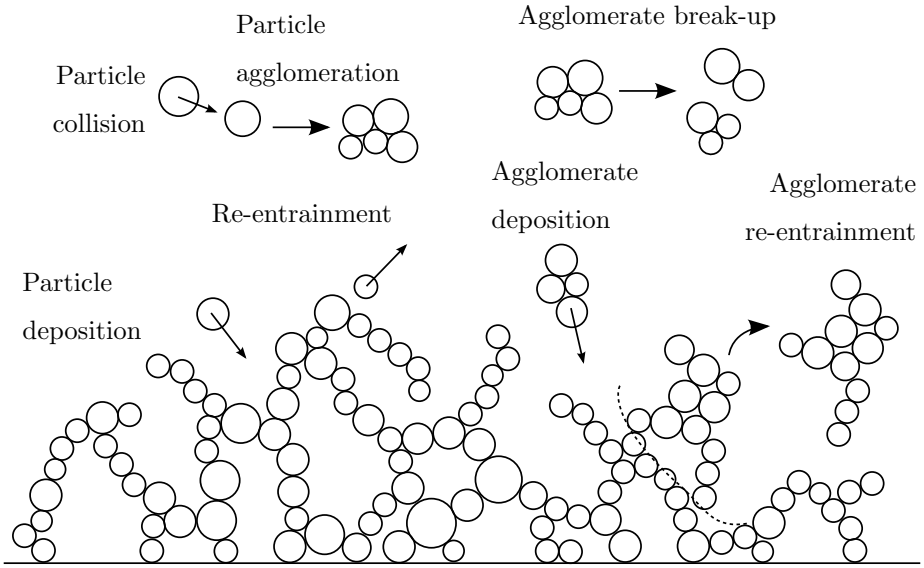

Figure 1: Overview of the different processes in the vicinity of a surface and away from a surface that are resolved directly by the soft-sphere DEM approach. The early stages of interest in this study are typically limited to particles colliding, particles agglomerating, agglomerates breaking up and a single particles depositing at surfaces.

2. Details on the numerical setup

2.1. Governing equations for fluid flow

The filtered LES equations governing unsteady, in-compressible, three-dimensional viscous fluid flow in a periodic domain with two-way coupling between particle and fluid phases are the continuity and momentum equations given by (1) and (2) respectively:

$$\frac{\partial \left(\alpha_{\mathrm{f}} \bar{u}_{\mathrm{i}}\right)}{\partial x_{\mathrm{i}}} = 0 \tag{1}$$

$$\frac{\partial \left(\alpha_{\mathrm{f}} \bar{u}_{\mathrm{i}}\right)}{\partial t} + \frac{\partial \left(\alpha_{\mathrm{f}} \bar{u}_{\mathrm{i}} \bar{u}_{\mathrm{j}}\right)}{\partial x_{\mathrm{j}}} = -\frac{\alpha_{\mathrm{f}}}{\rho_{\mathrm{f}}} \frac{\partial \bar{p}}{\partial x_{\mathrm{i}}} + \alpha_{\mathrm{f}} \frac{\partial}{\partial x_{\mathrm{j}}} \left(\left(\nu + \nu_{\mathrm{sgs}}\right) \frac{\partial \bar{u}_{\mathrm{i}}}{\partial x_{\mathrm{j}}} \right) + \beta \delta_{1,\mathrm{i}} + f \tag{2}$$

where α_{f} denoting the local fluid volume fraction and $\beta\delta_{1,\mathrm{i}}$ defines a momentum source term dynamically being changed to balance out the pressure gradient across the periodic domain. The sub-grid scale viscosity ν_{sgs} accounts for sub-grid scale turbulence and naturally approaches zero in the case of DNS. In this

study, focus is on LES where the sub-grid scale viscosity is modelled through the the wall-adapting local eddy-viscosity (WALE) model by Nicoud and Ducros [18]:

$$\nu_{\mathrm{sgs}} = \left(C_{\mathrm{w}} V^{1/3}\right)^2 \frac{\left(\bar{s}^{\mathrm{d}}_{\mathrm{ij}} \bar{s}^{\mathrm{d}}_{\mathrm{ij}}\right)^{3/2}}{\left(\bar{s}^{\mathrm{d}}_{\mathrm{ij}} \bar{s}^{\mathrm{d}}_{\mathrm{ij}}\right)^{5/2} + \left(\bar{s}^{\mathrm{d}}_{\mathrm{ij}} \bar{s}^{\mathrm{d}}_{\mathrm{ij}}\right)^{5/4}}, \tag{3}$$

where:

$$s^{\mathrm{d}}_{\mathrm{ij}} = \frac{1}{2}\left(\bar{g}^2_{\mathrm{ij}} + \bar{g}^2_{\mathrm{ji}}\right) - \frac{1}{3}\delta_{\mathrm{ij}} \bar{g}^2_{\mathrm{kk}}, \quad \bar{s}_{\mathrm{ij}} = \frac{1}{2}\left(\frac{\partial \bar{u}_{\mathrm{i}}}{\partial x_{\mathrm{j}}} + \frac{\partial \bar{u}_{\mathrm{j}}}{\partial x_{\mathrm{i}}}\right), \tag{4}$$

$$g_{\mathrm{ij}} = \frac{\partial \bar{u}_{\mathrm{i}}}{\partial x_{\mathrm{j}}}, \quad g^2_{\mathrm{ij}} = g_{\mathrm{ik}} g_{\mathrm{kj}} \tag{5}$$

with constant $C_{\mathrm{w}} = 0.325$ and where V is the local cell volume. Compared to the Smagorinsky-type models, the WALE model is more suited for wall-bounded flows, as the local sub-grid scale eddy-viscosity automatically goes to zero at the wall. Therefore, no dynamic constant adjusting or damping functions are needed to correct for walls.

2.2. Governing equations for particles

To model collisions of particles, the soft-sphere discrete element method (DEM) first proposed by Cundall and Strack [19] is used to track the translational and angular velocity throughout the simulations. For the i'th particle with mass m_{i}, radius r_{i} and mass moment of inertia $I_{\mathrm{i}} = (2/5) m_{\mathrm{i}} r^2_{\mathrm{i}}$, the position $\boldsymbol{x}_{\mathrm{i}}$ and angular velocity $\boldsymbol{\omega}_{\mathrm{i}}$ are governed by:

$$m_{\mathrm{i}} \frac{\mathrm{d}^2 \boldsymbol{x}_{\mathrm{i}}}{\mathrm{d}t^2} = \boldsymbol{F}_{\mathrm{i,con}} + \boldsymbol{F}_{\mathrm{i,fluid}} \tag{6}$$

$$I_{\mathrm{i}} \frac{\mathrm{d}\boldsymbol{\omega}_{\mathrm{i}}}{\mathrm{d}t} = \boldsymbol{M}_{\mathrm{i,con}} + \boldsymbol{M}_{\mathrm{i,roll}} + \boldsymbol{M}_{\mathrm{i,fluid}} \tag{7}$$

where the $\boldsymbol{F}_{\mathrm{con}}$ is a contact force upon collision and $\boldsymbol{F}_{\mathrm{fluid}}$ is the combined fluid force acting on the particle. In the angular momentum equation, $\boldsymbol{M}_{\mathrm{con}}$ is the contact torque by a tangential off-set between colliding particles, $\boldsymbol{M}_{\mathrm{roll}}$ is the adhesive rolling resistance torque and $\boldsymbol{M}_{\mathrm{fluid}}$ is the torque caused by interaction with the fluid phase.

2.2.1. Contact forces

Due to the small size of the particles of interest, the van der Waals force plays a dominant role in the collision process, which ultimately results in particles agglomerating and sticking to walls. Based on properties and size of the particles, particle deformation in contact region upon collision may be important in the description of the adhesive force. In this study, the van der Waals attractive force is modelled using the Johnson-Kendall-Roberts (JKR) adhesive model by Johnson et al. [20], which assumes particle deformation in the contact region to be important when describing the adhesive force. As noted by Tabor [21], the JKR model is valid when $\lambda_{\mathrm{T}} = \left(4R\gamma^2/(E^2 D_{\mathrm{min}}^3)\right)^{1/3} > 3$, where γ is the surface energy density, defining half the energy required to separate two particles in contact and D_{min} is the minimum separation distance between two particles, which is commonly assumed to be 1.65 Å [22, 23].

Using the JKR model, the normal contact force upon collision is balanced by a spring force $\boldsymbol{F}_{\mathrm{spring,n}}$ and an adhesive force $\boldsymbol{F}_{\mathrm{jkr,n}}$:

$$\boldsymbol{F}_{\mathrm{spring,n}} = -\frac{4E}{3R} a^3 \boldsymbol{n} \tag{8}$$

$$\boldsymbol{F}_{\mathrm{jkr,n}} = 4\sqrt{\pi\gamma E a^3}\boldsymbol{n} \tag{9}$$

where the effective Young's modulus E and effective radius R are given by:

$$\frac{1}{E} = \frac{1-\nu_{\mathrm{i}}^2}{E_{\mathrm{i}}} + \frac{1-\nu_{\mathrm{j}}^2}{E_{\mathrm{j}}}, \qquad \frac{1}{R} = \frac{1}{r_{\mathrm{i}}} + \frac{1}{r_{\mathrm{j}}} \tag{10}$$

and the contact radius a is the radius of contact area. In equilibrium state where $\boldsymbol{F}_{\mathrm{spring},} + \boldsymbol{F}_{\mathrm{jkr,n}} = 0$, the contact radius is $a = (9\pi\gamma R^2/E)^{1/3} = a_0$. When using DEM, the overlap distance δ_{n} between particle i and j with positions $\boldsymbol{x}_{\mathrm{i}}$ and $\boldsymbol{x}_{\mathrm{j}}$ is calculated as $\delta_{\mathrm{n}} = r_{\mathrm{i}} + r_{\mathrm{j}} - |\boldsymbol{x}_{\mathrm{i}} - \boldsymbol{x}_{\mathrm{j}}|$. For collisions following JKR theory, the relation between normal overlap δ_{n} and contact radius a is given by [23, 24]:

$$a^4 - 2R\delta_{\mathrm{n}} a^2 - \frac{4\pi\gamma}{E} R^2 a + R^2 \delta_{\mathrm{n}}^2 = 0 \tag{11}$$

which in this study is solved using the analytical solution derived by Parteli et al. [23]. Furthermore, the collision is damped by a normal damping force

$\boldsymbol{F}_{\mathrm{damp,n}}$ causing kinetic energy to be dissipated upon impact:

$$\boldsymbol{F}_{\mathrm{damp,n}} = -2\frac{5}{6}\beta\sqrt{S_{\mathrm{n}}m}\boldsymbol{v}_{\mathrm{n}} \tag{12}$$

with effective mass $m^{-1} = m_{\mathrm{i}}^{-1} + m_{\mathrm{j}}^{-1}$, $\boldsymbol{v}_{\mathrm{n}}$ denoting the relative normal velocity, β accounting for the kinetic energy lost upon impact through the coefficient of restitution e and S_{n} taking the properties of the particles into account:

$$\beta = \frac{\ln(e)}{\sqrt{\ln^2(e) + \pi^2}} \tag{13}$$

$$S_{\mathrm{n}} = 2E\sqrt{R\delta_{\mathrm{n}}} \tag{14}$$

where e is material property. Due relatively low collision velocities, plastic deformation of particle material is not expected to be important. In the tangential direction, the spring force is given by:

$$\boldsymbol{F}_{\mathrm{spring,t}} = -S_{\mathrm{t}}\Delta s_{\mathrm{t}} \tag{15}$$

where Δs_{t} is the tangential overlap and S_{t} takes particle properties into account through $S_{\mathrm{t}} = 8G\sqrt{R\delta_{\mathrm{n}}}$ with effective shear modulus G:

$$\frac{1}{G} = \frac{2-\nu_{\mathrm{i}}}{G_{\mathrm{i}}} + \frac{2-\nu_{\mathrm{j}}}{G_{\mathrm{j}}} \tag{16}$$

Like in the normal direction, energy is dissipated in the tangential direction, described by a tangential damping force:

$$\boldsymbol{F}_{\mathrm{damp,t}} = -2\sqrt{\frac{5}{6}}\beta\sqrt{S_{\mathrm{t}}m}\boldsymbol{v}_{\mathrm{t}} \tag{17}$$

where $\boldsymbol{v}_{\mathrm{t}}$ is the tangential relative velocity. As suggested by Thornton [25], Thornton and Yin [26], the total tangential force is in the case of JKR adhesion truncated to fulfil $|\boldsymbol{F}_{\mathrm{con,t}}| \leq \mu_{\mathrm{s}}|F_{\mathrm{N}} + 2F_{\mathrm{C}}|$ with μ_{s} and F_{C} being the sliding friction coefficient and the critical force required to separated agglomerated particles respectively.

2.2.2. Contact torques

In the case of adhesive particles, the formation of agglomerates and motion of particles on a surface tend to be dominated by particles rolling while particles

sliding and twisting play negligible roles due to the small particle inertia [27, 28]. As a consequence of the deformed contact region described through JKR theory, the rolling motion differs from that of non-adhesive particles.

In the case of adhesive forces in the contact region between two particles or a particle and a wall, the point of contact stays behind the centre of mass projected onto the surface, which results in a torque opposing motion. This rolling resistance torque acts to obtain the equilibrium condition where the projected centre of mass and centre of contact are coincident. The rolling resistance torque is commonly described as proportional to the rolling displacement ξ, which is found by integrating the rolling velocity $\boldsymbol{v}_\mathrm{r}$:

$$\xi = \left(\int_{t_0}^{t_1} \boldsymbol{v}_\mathrm{r}(t) \mathrm{d}t \right) \cdot \boldsymbol{t}_\mathrm{r} \tag{18}$$

where $\boldsymbol{t}_\mathrm{r} = \boldsymbol{v}_\mathrm{r}/|\boldsymbol{v}_\mathrm{r}$ is the direction of rolling. Based on the instantaneous rolling displacement ξ, the rolling resistance torque opposing motion is given by [29, 30]:

$$M_\mathrm{r} = \begin{cases} k_\mathrm{r}\xi & \text{if } \xi < \xi_\mathrm{crit} \\ k_\mathrm{r}\xi_\mathrm{crit} & \text{if } \xi \geq \xi_\mathrm{crit} \end{cases} \tag{19}$$

where the rolling stiffness is given by $k_\mathrm{r} = 4F_\mathrm{C} \left(a/a_0\right)^{3/2}$. When the particle is rolled a distance longer than a critical rolling displacement ξ_crit, the particle material slips and a new equilibrium contact region is found. The studies by Dominik and Tielens [29, 30] suggests that after rolling displacement reaches a critical value ξ_crit, the rolling resistance torque is constant. Based on experiments, Krijt et al. [31] suggests this critical rolling displacement to be linked to the equilibrium contact radius a_0 and a material dependent adhesion hysteresis parameter $\Delta\gamma/\gamma$ through:

$$\xi_\mathrm{crit} = \frac{a_0}{12} \frac{\Delta\gamma}{\gamma} \tag{20}$$

A value $\Delta\gamma/\gamma = 0.5$ representing a typical value [31] is used throughout this study.

2.3. Non-dimensional groups

The results are reported based on a set of non-dimensional groups that govern different aspects of particle transport, particle collision and subsequently the agglomeration and deposition processes.

The numbers governing the transport of particles are the Reynolds number $\mathrm{Re} = U \cdot D/\nu$, the dimensionless particle size $\epsilon = d_\mathrm{p}/D$, the particle to fluid density ratio $\chi = \rho_\mathrm{p}/\rho_\mathrm{f}$, the Stokes number $\mathrm{St} = \rho_\mathrm{p} d_\mathrm{p}^2 U/(18\mu D) = \chi\epsilon^2\mathrm{Re}/18$ and the particle volume fraction defining the volume occupied by particles in the fluid domain $\phi = \sum_{n=1}^{N} V_\mathrm{p}/(\sum_{n=1}^{N} V_\mathrm{p} + V_\mathrm{f})$. The importance of gravity is described through the Froude number $\mathrm{Fr} = U/\sqrt{g_\mathrm{r} d_\mathrm{p}}$, where $g_\mathrm{r} = (1 - 1/\chi)g$ is the buoyancy corrected gravity acceleration.

Likewise, the collision and agglomeration processes are governed by a set of non-dimensional groups. The stiffness of a common collision is described by making the effective Young's modulus dimensionless using the particle density, bulk velocity and particle density forming $\lambda = E/(\rho_\mathrm{p} U^2)$. Likewise, to describe the sticking behaviour upon impact, the surface energy density, describing the strength of the adhesive force, is made non-dimensional by the particle density, bulk velocity and particle diameter, forming $\mathrm{Ad} = \gamma/(\rho_\mathrm{p} U^2 d_\mathrm{p})$.

Due to stiffness of most common materials, the time step size required to resolve particle collisions is typically in the order of nano seconds. A common approach to deal with the low time step sizes is to reduce the particle stiffness several orders of magnitude making collisions take place over longer time periods. For non-adhesive particles colliding without any plastic deformation, the rebound velocity is solely a function of velocity before collision and the coefficient of restitution. However, for collisions involving adhesive particles, the reduced particle stiffness has to be balanced by a reduction in adhesive inter-molecular force so that the collision outcome remains the same. In this study, the high particle stiffness is reduced by decreasing the effective Young's

modulus while modifying the surface energy density as:

$$\gamma_{\mathrm{mod}} = \gamma \left(\frac{E_{\mathrm{mod}}}{E} \right)^{2/5} \tag{21}$$

or in terms of the dimensionless elasticity parameter λ and adhesiveness parameter Ad:

$$\mathrm{Ad}_{\mathrm{mod}} = \mathrm{Ad} \left(\frac{\lambda_{\mathrm{mod}}}{\lambda} \right)^{2/5} \tag{22}$$

which is shown by Hærvig et al. [11] to make the collision outcome independent of a reduction in Young's modulus. For particles colliding in a viscous fluid, the fluid being forced away in the contact prior to collision may have a non-negligible effect on the rebound velocity [32, 33]. This importance of this effect is described through the collision Stokes number $\mathrm{St}^* = (m_{\mathrm{p}} + C_{\mathrm{M}} m_{\mathrm{f}})\, v/(6\pi\mu r_{\mathrm{p}})$, where $C_{\mathrm{M}} = 0.5$ is the added mass coefficient for spheres and v denotes the velocity before being affected by the surface. For solid particles colliding with $\mathrm{St}^* < 10$, Legendre et al. [34] suggests all energy to be dissipated while for higher values of St^*, this effect quickly becomes negligible.

2.4. Particle-fluid interaction

The fluid force governing the transport of particles $\boldsymbol{F}_{\mathrm{fluid}}$ in equation (6) is obtained by point-force approximations due to the large number of particles involved. The fluid force is split up into different contributions that include: a fluid drag force, Saffman lift force due to local shear in the flow field, Magnus lift force due to local relative angular velocity between particle and fluid, a buoyancy-corrected gravity force, a added mass force due to acceleration of nearby fluid, a Basset history force due to delay in boundary layer build-up and a Brownian motion force due to random collisions with fluid molecules.

Due to the large density ratio between particles and air, typically $\chi = \rho_{\mathrm{p}}/\rho_{\mathrm{f}} > 1000$, the added mass and history forces are neglected in the present study as suggested by Dritselis [35], Armenio and Fiorotto [36].

Also, gravity plays a minor role compared to drag for the small particles considered. As shown by Marshall [37], the ratio of gravity to Stokes drag can be

approximated by combining the dimensionless particle diameter and the Froude number as: $F_\mathrm{g}/F_\mathrm{d} = \mathcal{O}\left(\epsilon\ \mathrm{Fr}^2\right)^{-1}$. For particles investigated in this study, this ratio is $F_\mathrm{g}/F_\mathrm{d} = \mathcal{O}\left(10^{-2}\right)$ and thus gravity is expected to play a negligible role. Furthermore, molecular effects due to Brownian motion are neglected as the particles considered are several orders of magnitude larger than fluid molecules. Moreover, it is assumed that the mean free path of fluid molecules is much smaller than the particle size ($\mathrm{Kn} \ll 1$), so that the standard continuum assumption is valid and the effect of surface slip is negligible.

2.4.1. Fluid force contributions

As inter-particle van der Waals forces cause agglomerates to form and particles to deposit, the particle volume fraction α_p increases locally. When particles agglomerate, the individual particles in the agglomerate are affected by fluid forces that are significantly different from the fluid force on single particles in dilute flows. Therefore, a drag formulation taking the presence of surrounding particles into account is used. In this study, the Lattice-Boltzmann-based drag formulation suggested by Hill et al. [14, 15] and later modified by Benyahia et al. [38] to cover particle Reynolds numbers up to 100 and particle volume fractions approaching the closed-pack solution is used.

For particles in the viscous sub-layer, where strong velocity gradients exist, Saffman lift force is expected to be important as suggested by McLaughlin [39]. Furthermore, Magnus lift due to relative angular velocity between particle and fluid is included as off-centre collisions may result in particles rebounding with non-negligible angular velocities. To model these fluid force contributions, the expressions derived by Kurose and Komori [40] and McLaughlin [41] are used.

3. Results and validation

3.1. Fluid domain and discretisation

To make the results independent of stream-wise boundaries, the fluid domain is made periodic with a length longer than the elongated coherent turbulence

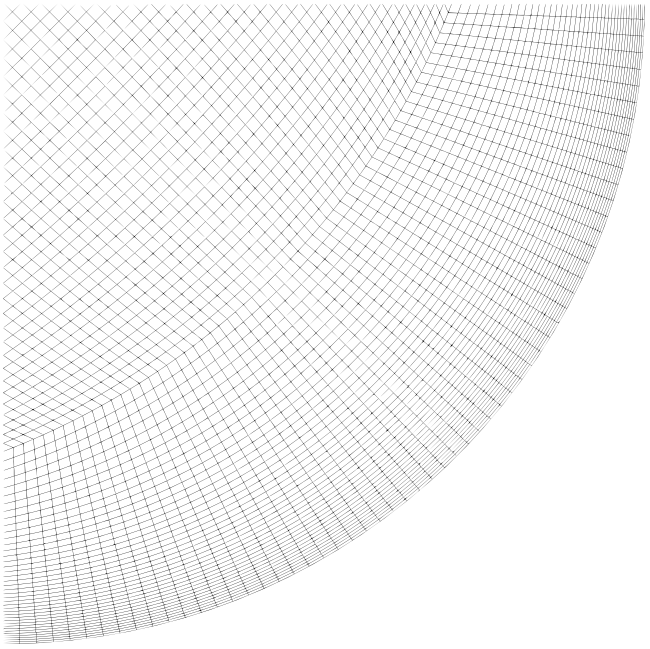

Figure 2: Mesh topology visualised by a quarter of the cross-sectional plane.

structures in the boundary layer extending around $L_x^+ \approx 1000$ [42]. In this study, a domain length of $L/D = 4$, corresponding to $L_x^+ \approx 2500$ in viscous units, is chosen to make sure no coherent structures extend throughout the domain. Thus, the turbulence statistics are not affected by the size of the computational domain. A quarter of the cross-sectional mesh topology is shown in figure 2. As the agglomeration formation process takes place over streamwise distances significantly longer than $L/D = 4$, the DEM domain is made periodic as well. In that way, the overall particle volume fraction ϕ stays constant throughout the simulation. This approach gives detailed information on the mechanisms governing agglomeration and deposition and how changes in fluid/particle properties affect early stages of agglomeration and deposition. Later stages of the deposition process where bridges and layers of multiple particles form, see figure 1, would require particles to be added throughout the simulation or a significantly higher initial particle concentration, which would alter the early stages of agglomeration and deposition processes.

Table 1: Details of the three different meshes with θ, r and x denoting circumferential, radial and axial directions respectively. The mesh topology is shown in figure 2.

Resolution	$(N_\theta, N_\mathrm{r}, N_\mathrm{x})$	$\Delta\theta^+_\mathrm{max}$	Δx^+_max
Coarse	(160,90,160)	12	15
Medium	(200,110,200)	10	12.5
Fine	(240,140,240)	8	10

3.2. Validation of flow field

To validate the statistics of the flow field without particles added, the boundary layer velocity profile is compared for the different meshes listed in table 1. The various grid resolutions are compared to experiments by den Toonder and Nieuwstadt [43] and boundary layer theory. Parameters for the different meshes are listed in table 1. In this section, the time-averaged turbulent flow obtained by LES simulations without particles is compared to theory to ensure reasonable accuracy compared to experimental data and theory. The time-averaged flow field is found by averaging over a time period of $t^+ = t \cdot U/D = 400$ after which the mean flow field statistics are found to be independent of time. Figure 3 shows how the numerical simulations compare to boundary layer theory and experiments at $\mathrm{Re} = 10,000$. As seen in figure 3, the more resolving LES simulations approach the experiment by den Toonder and Nieuwstadt [43].

3.3. Particle properties

Particles with $d_\mathrm{p} = 10$ µm and $\rho_\mathrm{p} = 2500$ kg/m^3 are transported in pipe flow with $D = 40$ mm and mean velocity $U = 5$ m/s so that $\mathrm{Re} = U \cdot D/\nu \approx 10,000$, $\mathrm{St} = \rho_\mathrm{p} d_\mathrm{p}^2 U/(18\mu D) \approx 0.1$ and $\epsilon = d_\mathrm{p}/D = 0.25 \cdot 10^{-3}$.

The particles are affected by an inter-particle adhesive force characterised by a surface energy density and develop a flattened contact region as predicted by JKR theory. The particles have stiffness and adhesiveness such that $\lambda = E/(\rho_\mathrm{p} U^2) \approx 500 \cdot 10^3$, $\mathrm{Ad} = \gamma/(\rho_\mathrm{p} U^2 d_\mathrm{p}) \approx 0.08$ and coefficient of

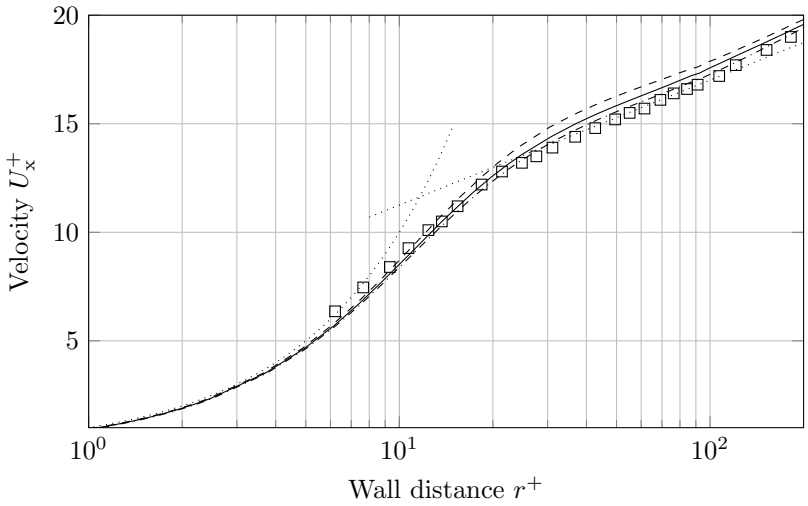

Figure 3: Time-averaged turbulent boundary layer velocity profile for $\mathrm{Re} = UD/\nu = 10,000$ for different mesh resolutions, see table 1: (- - -) Coarse resolution LES; (——) Medium resolution LES; (-·-·-) Fine resolution LES; (·····) Viscous sub-layer with $U_x^+ = r^+$ and log-law layer with $U_x^+ = 2.5\ln(r^+) + 5.5$; □ Experiment for $\mathrm{Re} = 10,000$ by den Toonder and Nieuwstadt [43].

restitution $e \approx 0.3$. The particles are initially placed randomly throughout the turbulent flow without any particles being in contact. Instead of using a more or less sophisticated correlation to prescribe the initial velocity of particles, the particles are inserted with zero velocity in the present study. A constant volume fraction $\phi = 10^{-3}$ is used in all simulations.

However, due to the significant difference in particle to pipe size ratio $\epsilon = d_p/D = 0.25 \cdot 10^{-6}$, it takes $\approx 0.4 \cdot 10^9$ particles to get a volume fraction $\phi = 0.001$, making the simulations practically computationally impossible for the DEM method. Instead, the particle size is increased from $\epsilon = 0.25 \cdot 10^{-3}$ to $\epsilon = 5 \cdot 10^{-3}$, while scaling the other non-dimensional groups to get the parameters listed above. For example, to ensure the artificially larger particles have the same particle to fluid response time, the density ratio χ is scaled according to $\mathrm{St} = \chi\epsilon^2\mathrm{Re}/18$. Furthermore, as the adhesiveness parameter is a function of particle diameter, the surface energy density γ is scaled as well so

that the adhesive behaviour remains the same despite an increase in particle size.

3.4. Overview of simulations

The following gives an overview of the different simulations carried out in the present study. The simulation parameters are summarised in terms of non-dimensional numbers in table 2.

Simulation no. 1–21. Depending on the Stokes number, the particles will be affected by different turbulence scales. As the Stokes number approaches zero, the particles will be affected by increasingly smaller eddies. In this study where LES is used, it is important that particles are unaffected by the eddies not being resolved. Therefore, simulations with varying Stokes number $\mathrm{St} = 0.4 \cdot 2^x$, $x = 0 \ldots 6$ and carried out using the three meshes listed in table 1.

Simulation no. 22–28. As already mentioned, the agglomeration processes considered in this study have elasticity parameter $\lambda \approx 500 \cdot 10^3$. Using this value, particle-particle and particle-wall collisions happen over time intervals in the order of nano seconds. To reduce computational time, a modified elasticity parameter is introduced: $\lambda_{\mathrm{mod}} = \lambda \cdot 0.001 = 500$. By reducing the elasticity parameter, the particles behave more adhesive. Therefore, to ensure the collision outcome stays independent of reduction in elasticity parameter, the criterion in (22) is used to reduce the adhesiveness parameter so that $\mathrm{Ad}_{\mathrm{mod}} = 0.08 \cdot 0.001^{2/5} = 0.005$. However, as noted in the study, introducing a lower adhesiveness parameter also reduces the critical force $F_{\mathrm{C}} = 3\pi R\gamma$ required to separate two agglomerated particles. Therefore, simulations 22–28 are carried out with $\lambda_{\mathrm{mod}} = \lambda/100$ instead of $\lambda_{\mathrm{mod}} = \lambda/1000$ to ensure the agglomeration rate is in fact independent of a reduction in elasticity and adhesiveness parameter.

Simulation no. 29-42. The purpose of simulation 29–42 is to investigate the transition from particles acting almost non-adhesive to particles being highly

Table 2: Details on the simulations in terms of non-dimensional groups: Flow Reynolds number $\mathrm{Re} = U \cdot D/\nu$, particle size $\epsilon = d_\mathrm{p}/D$, Stokes number $\mathrm{St} = \chi\epsilon^2\mathrm{Re}/18$, elasticity parameter $\lambda = E/(\rho_\mathrm{p}U^2)$, adhesiveness parameter $\mathrm{Ad} = \gamma/(\rho_\mathrm{p}U^2 d_\mathrm{p})$, coefficient of restitution e, particle volume fraction ϕ and LES resolution (see table 1). The integer x is used to describe a range of simulation parameters.

No.	x	Re	ϵ	St	λ	Ad	e	ϕ	LES res.
1–7	$0\,..\,6$	10^4	0.005	$0.4 \cdot 2^x$	500	0.05	0.3	10^{-3}	Coarse
8–14	$0\,..\,6$	10^4	0.005	$0.4 \cdot 2^x$	500	0.05	0.3	10^{-3}	Medium
15–21	$0\,..\,6$	10^4	0.005	$0.4 \cdot 2^x$	500	0.05	0.3	10^{-3}	Fine
22–28	$0\,..\,6$	10^4	0.005	$0.4 \cdot 2^x$	5000	$0.05 \cdot 10^{2/5}$	0.3	10^{-3}	Medium
29–35	$0\,..\,6$	10^4	0.005	1	500	$0.001 \cdot 2^x$	0.3	10^{-3}	Medium
36–42	$0\,..\,6$	10^4	0.005	10	500	$0.001 \cdot 2^x$	0.3	10^{-3}	Medium

adhesive at constant Stokes numbers. For this purpose, the adhesive parameter is varied in the range 0.001 to 0.064 at a constant Stokes number $\mathrm{St} = 1$ (simulations 29–35). Similar simulations are carried out for $\mathrm{St} = 10$ (simulations 36–42).

3.5. Effect of sub-grid scale turbulence eddies on particle agglomeration

As the smallest eddy scales are modelled by a sgs-model, it is important that these unresolved scales do not affect particle motion and subsequently agglomeration and deposition. Ultimately, as particles with sufficiently low response time, e.g. tracer particles, would respond to all turbulence scales, a DNS solution would be required in this case. However, as pointed out by Armenio [44], particles with finite mass do not respond to smaller turbulence scales, suggesting LES to be an appreciate method to investigate particles interactions in a turbulent flow. Figure 4 shows how the agglomeration rate by the average number of particles in each agglomerate as function of time for different particle Stokes numbers. As the figure shows, particles with $\mathrm{St} = \mathcal{O}(10)$ are almost unaffected by changes in mesh resolution. This suggests that these particles are unaffected by eddies smaller than the grid size of the coarse mesh. For particles with $\mathrm{St} = \mathcal{O}(1)$, there is pronounced difference between the coarse and medium mesh resolutions, suggesting particles with $\mathrm{St} = \mathcal{O}(1)$ to respond to

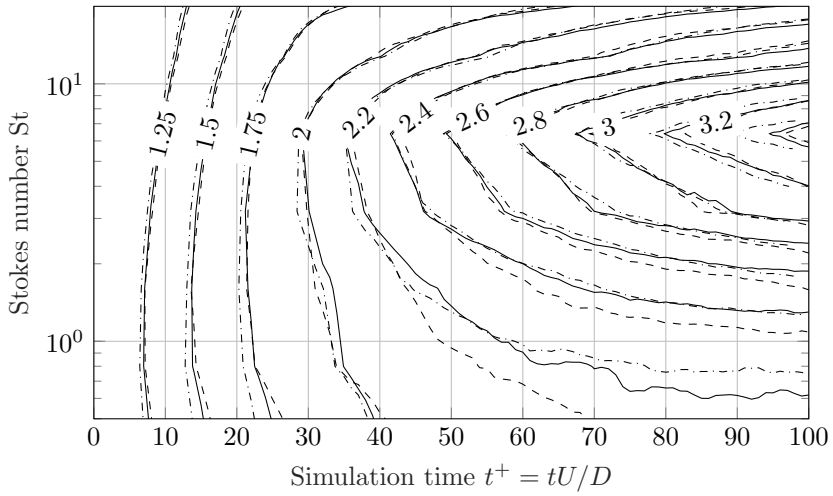

Figure 4: Effect of mesh resolution, see table 1, and Stokes number on particle agglomeration behaviour visualised by the average number of particles per agglomerate. As no particles are in contact at $t^+ = 0$, the average number of particles is 1. See simulation no. 1–21 in table 2 for simulation parameters: (- - -) Coarse resolution LES; (——) Medium resolution LES; (-·-·-) Fine resolution LES.

eddies not being resolved by the coarsest mesh. The difference is insignificant when comparing the medium and fine mesh resolutions, suggesting that the particles are almost unaffected by the smaller eddies not being resolved by the medium resolution mesh. As a consequence, the medium resolution mesh from table 1 is used to investigate how changes particle response time and adhesiveness affect the agglomeration rate.

3.6. Effect of introducing softer particles

In the present study, the particle stiffness is reduced by a factor 1000 from $\lambda = 500 \cdot 10^3$ to $\lambda_{\text{mod}} = 500$ in order to increase collision duration and consequently allow for an increased DEM time step size. The result is smaller difference between fluid time step size δt_{f} and particle time step size δt_{col} that decrease the computational time. In order for the collision outcome (sticking/rebounding) to remain the same despite a reduced particle stiffness, the particle adhesiveness is modified using the criterion given in (22), giving a

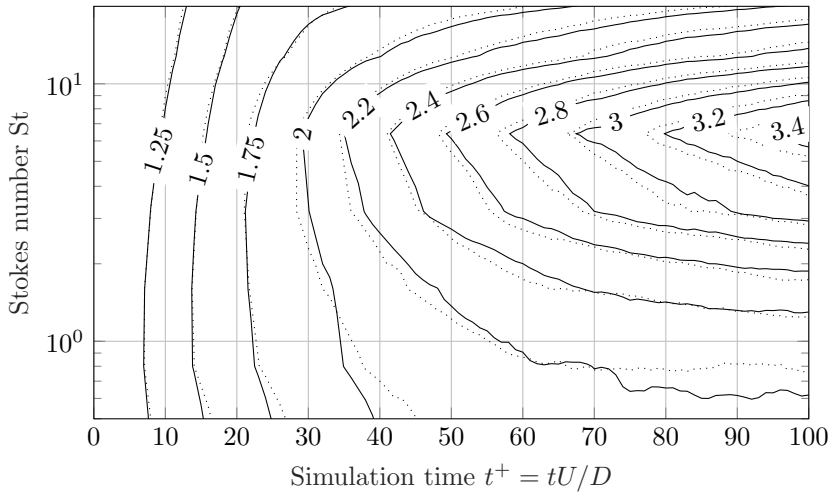

Figure 5: Effect of introducing softer particles using the criterion in (22). Contours show particle agglomeration rate visualised by the average number of particles contained in each agglomerate for particle elasticity parameters $\lambda = 500$ and $\lambda = 5000$. See simulation no. 8–14 and 22–28 in table 2 for simulation parameters: (——) $\lambda_1 = 500$, $\mathrm{Ad}_1 = 0.05$; (·····) $\lambda_2 = 5000$, $\mathrm{Ad}_2 = \mathrm{Ad}_1 \cdot (\lambda_2/\lambda_1)^{2/5}$.

modified collision duration $\Delta t_{\mathrm{col,mod}} = \Delta t_{\mathrm{col}} \left(\lambda/\lambda_{\mathrm{mod}}\right)^{2/5}$ [11]. To ensure that the agglomeration process is in fact independent of this change, an additional set of simulations with $\lambda = 5000$ is carried out. Figure 5 shows results for $\lambda_1 = 500$ and $\lambda_2 = 5000$ with adhesiveness parameters $\mathrm{Ad}_1 = 0.05$ and $\mathrm{Ad}_2 = \mathrm{Ad}_1(\lambda_2/\lambda_1)^{2/5}$. As figure 5 shows, the agglomeration process is almost independent of a change in elasticity parameter from $\lambda = 500$ to $\lambda = 5000$ when reducing the adhesiveness parameter by (22) for particles with Stokes numbers in the range $\mathrm{St} = 0.4$ to $\mathrm{St} = 25.6$.

3.7. Effect of particle Stokes number on agglomeration and deposition

Depending on the Stokes number, the agglomeration process is governed by different distinct mechanisms. At sufficiently low Stokes numbers $\mathrm{St} \ll 1$, the particles behave as tracer particles and respond to all turbulence scales. That is, collisions happen due to the finite size of particles that all follow different fluid streamlines. At sufficiently high Stokes numbers $\mathrm{St} \gg 1$, the particle velocity is

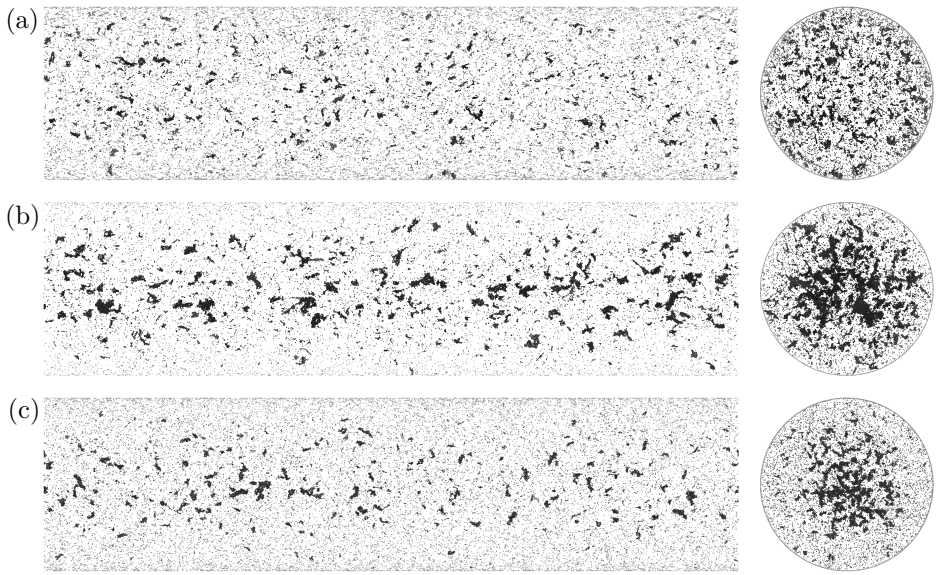

Figure 6: Agglomerating and depositing behaviour at time $t^+ = tU/D = 100$: (a) St = 0.8, see simulation no. 9 in table 2; (b) St = 6.4, see simulation no. 12 in table 2; (c) St = 25.6, see simulation no. 14 in table 2. To distinguish between moving particles and deposited particles, the particles are coloured according to their velocity magnitude. White corresponds to low velocity and black corresponds to high velocity.

only weakly correlated with the local fluid velocity. Figure 6 gives an overview of the agglomerates formed at time $t^+ = 100$ for Stokes numbers of 0.8, 6.4 and 25.6. As shown in figure 6, the agglomeration rate is highest at intermediate Stokes numbers where larger agglomerates are being formed in the centre of the pipe, see 6(b). This can be explained by the increased collision frequency when the accelerative-correlated collision mechanism is dominant. Figure 7 gives an overview of the agglomeration process in terms of particle location. Figure 7 shows the radial concentration of particles in terms of local volume fraction ϕ_r normalised by the overall particle volume fraction ϕ in different radial intervals r normalised by the pipe radius R at different times for simulation no. 9 in table 2. As shown in figure 7, there is an increasing amount of particles sticking to the wall, while the concentration profile throughout the pipe remains relatively constant. This can be explained by the low Stokes number where $\tau_\mathrm{p} < \tau_\mathrm{f}$ causing

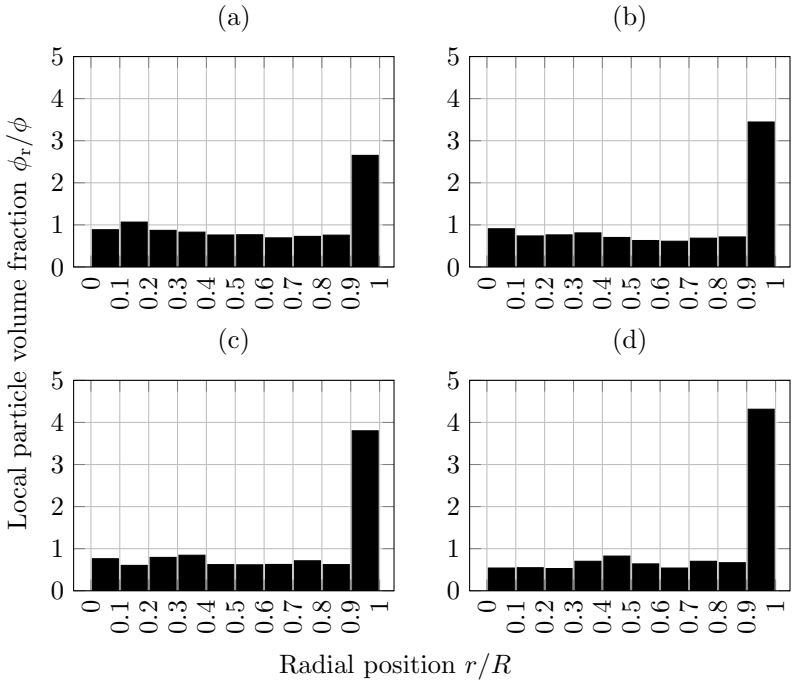

Figure 7: Local particle volume fraction ϕ_r in radial intervals of $r/R = 0.1$ normalised by the overall particle volume fraction ϕ at different times. Stokes number St = 0.8, see simulation no. 9 in table 2 for simulation parameters: (a) $t^+ = tU/D = 25$; (b) $t^+ = tU/D = 50$; (c) $t^+ = tU/D = 75$; (d) $t^+ = tU/D = 100$.

particles to respond to most of the eddies resolved in turbulent flow. Figure 8 shows how the particle concentration profile is affected by an increase in Stokes number. At a slightly higher Stokes number St = 6.4, particle accumulate in the centre of the pipe and near the wall. This phenomenon is explained by an increased collision frequency, causing agglomerates to form quickly. As agglomerates are formed, the effective response time for agglomerates is greatly increased, causing agglomerates to drift towards the centre of the pipe due to the shear velocity profile. Figure 9 shows the radial particle concentration profile for higher Stokes number of St = 25.6. At a higher Stokes number, the primary particles are expected to almost unaffected by turbulent fluctuations so that the average flow field cause particles to drift towards the centre of the pipe. However, compared to the lower Stokes number in figure 7, more particles

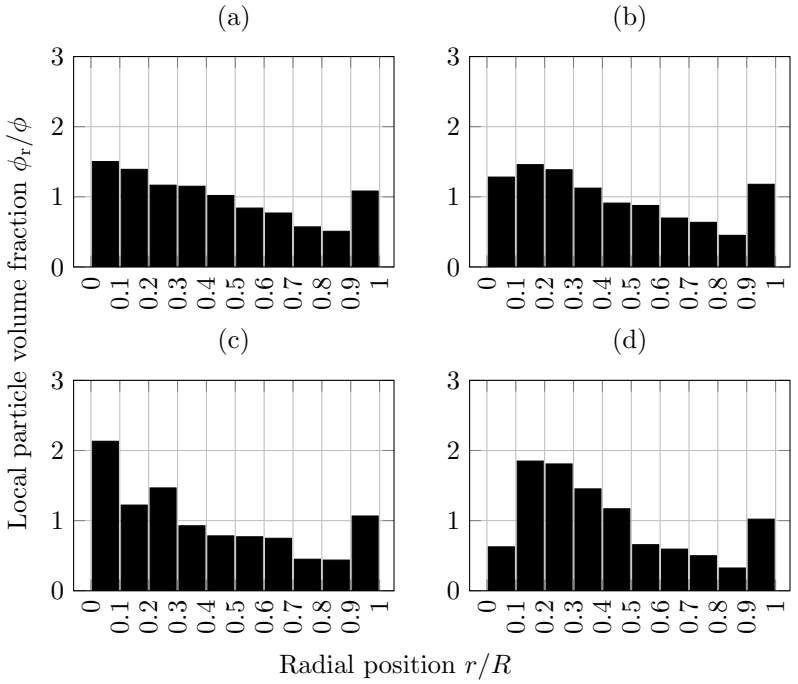

Figure 8: Local particle volume fraction ϕ_r in radial intervals of $r/R = 0.1$ normalised by the overall particle volume fraction ϕ at different times. Stokes number St = 6.4, see simulation no. 12 in table 2 for simulation parameters: (a) $t^+ = tU/D = 25$; (b) $t^+ = tU/D = 50$; (c) $t^+ = tU/D = 75$; (d) $t^+ = tU/D = 100$.

adhere to the surface of the pipe. This can be explained by the particles not responding as quickly to the high velocity gradient close to the wall, causing particles to move through the boundary layer and adhere to the wall.

3.8. Effect of particle adhesiveness on agglomeration

In the following, the effect of increased particle adhesiveness is investigated. The surface energy density γ is varied, resulting in adhesiveness parameters in the range Ad = 0.001 to Ad = 0.064, covering particles that range from weakly to highly adhesive. Figure 10 gives an overview of how the adhesiveness parameter changes the agglomerating behaviour for particles with St = 1. As figure 10(a) shows, the weakly adhesive particles only form smaller agglomerates in the centre of the tube and are significantly more uniformly distributed than

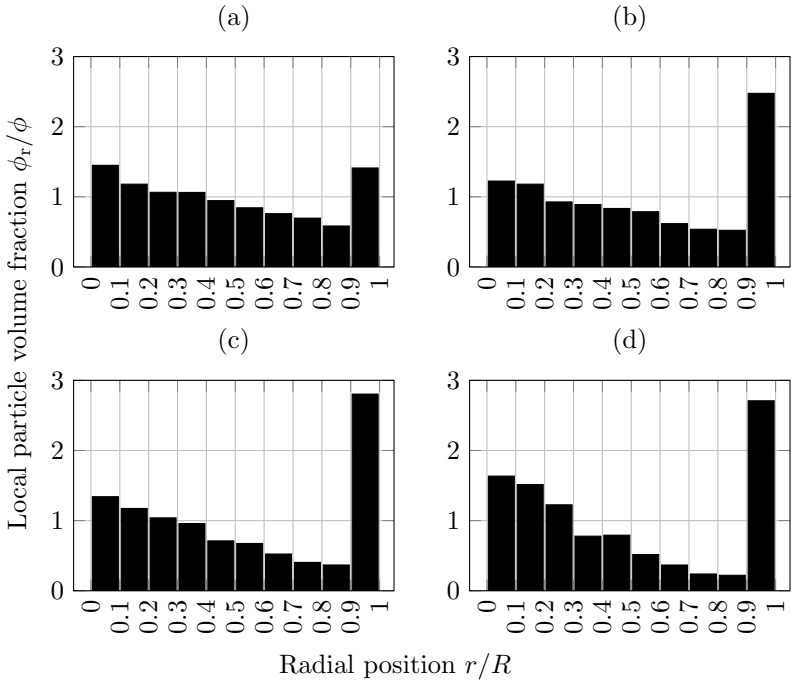

Figure 9: Local particle volume fraction ϕ_r in radial intervals of $r/R = 0.1$ normalised by the overall particle volume fraction ϕ at different times. Stokes number St = 25.6, see simulation no. 14 in table 2 for simulation parameters: (a) $t^+ = tU/D = 25$; (b) $t^+ = tU/D = 50$; (c) $t^+ = tU/D = 75$; (d) $t^+ = tU/D = 100$.

the more adhesive particles in figure 10(b) and 10(c). Figure 11 shows the average number of particles per agglomerate as function of simulation time at different adhesiveness parameters. As figure 11 shows, the weakly adhesive particles with Ad = 0.001 are in average contained in agglomerates consisting of less than 1.025 particles. Even for non-adhesive particles with Ad = 0, a non-zero average agglomeration size is expected due to the finite collision duration, causing particles to be in contact for short durations before they separate again due to repulsive contact forces. At slightly higher adhesiveness parameters, significant agglomeration is observed with agglomerates being present throughout the flow field. Figure 12 shows how an increase in adhesiveness parameter from Ad = 0.002 to Ad = 0.064 affects the local particle concentration. As depicted in figure 12, an increasing amount of particles adhere

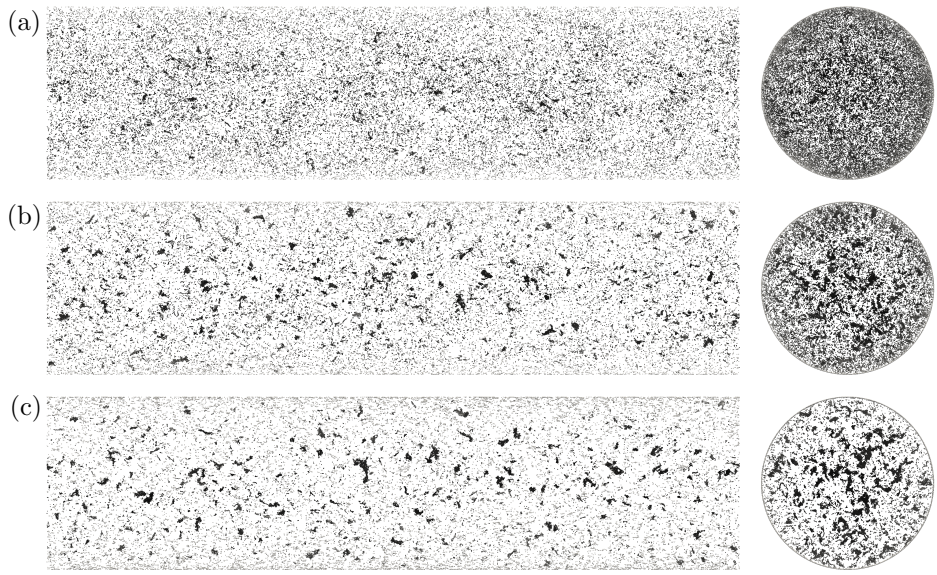

Figure 10: Overview of agglomerating behaviour of mono-dispersed particles with different adhesiveness parameters at time $t^+ = tU/D = 100$: (a) Ad = 0.016; (b) Ad = 0.032; (c) Ad = 0.064. To distinguish between moving particles and deposited particles, the particles are coloured according to their velocity. White corresponds to low velocity and black corresponds to high velocity.

to the wall when the adhesiveness parameter is increased.

4. Conclusions and discussion

Numerical results of how micron-sized agglomerate and deposit in a periodic, fully-developed turbulent pipe flow with Re = 10000 flow are presented. In this study, focus is on the first stages of agglomeration and deposition up to $t^+ = tU/D = 100$.

Firstly, Large Eddy Simulations (LES) are compared to experiments from literate in terms of boundary layer profile. With particles added, the effect of sub-grid scale fluctuations are linked to the Stokes number to ensure particle motion is independent of the unresolved velocity fluctuations. Fluid-particle interactions are based on the point-particle approach while particle-particle and particle-wall interactions are resolved directly using the soft-sphere DEM

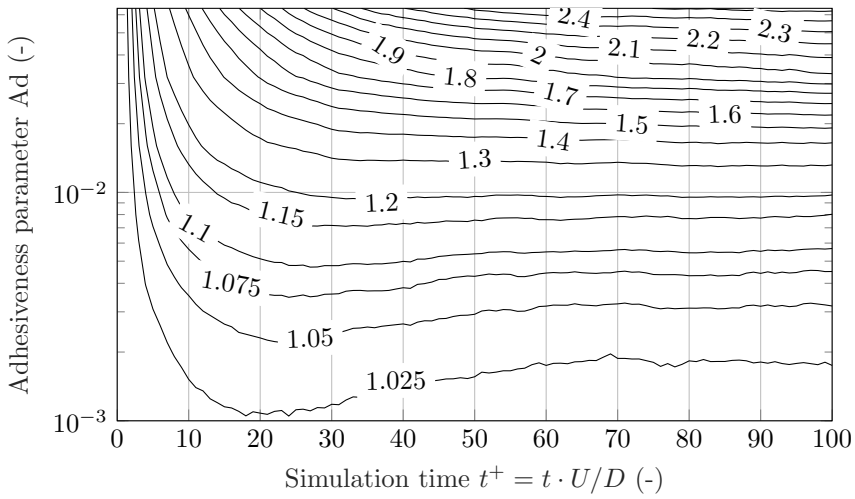

Figure 11: Effect of particle adhesiveness parameter $\mathrm{Ad} = \gamma/(\rho_\mathrm{p} U^2 d_\mathrm{p})$ on particle agglomeration behaviour visualised by the average number of particles in each agglomerate, see simulation no. 29–35 in table 2 for simulation parameters.

approach relying on the physical properties of the particles, where the adhesive behaviour is described through JKR theory.

Secondly, the effects of changes in particle response time on the agglomeration and deposition rates are investigated. By varying the Stokes number from 0.4 to 25.6, the results show a peak in agglomeration rate at $\mathrm{St} = 6.4$, which can be explained by a high collision frequency. For a low Stokes number of $\mathrm{St} = 0.8$, agglomerates are found throughout the flow field. Due to low particle response time, the particle concentration is close to uniform throughout the tube with a increase in particle concentration near the wall due to particle being captured by the wall. At a higher Stokes number $\mathrm{St} = 6.4$, the particles tend to accumulate in the centre of the tube. This is expected to be caused by the high collision rate that quickly form agglomerates that increase the effective particle size so that the Saffman lift force dominates their radial motion causing them to move towards the centre of the pipe. At an even higher Stokes number $\mathrm{St} = 25.6$, the particles are observed to accumulate in the centre of the pipe as well.

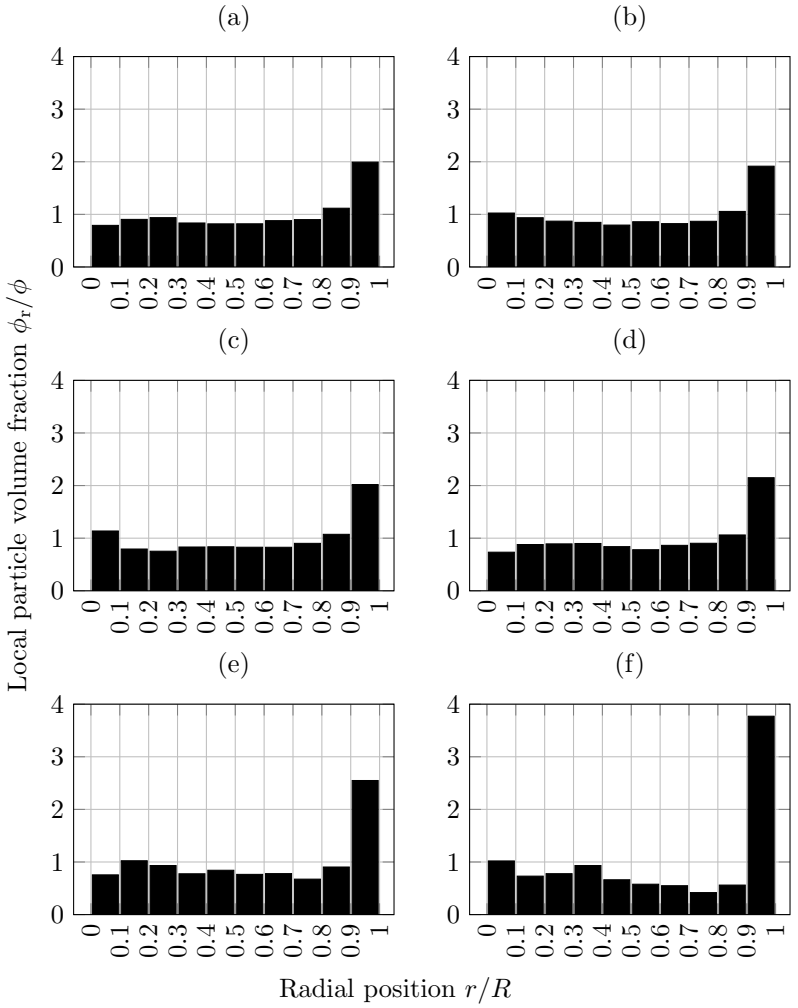

Figure 12: Local particle volume fraction ϕ_r in radial intervals of $r/R = 0.1$ normalised by the overall particle volume fraction ϕ at $t^+ = 100$. Varying adhesiveness parameter, see simulation no. 30–35 in table 2 for simulation parameters: (a) Ad = 0.002; (b) Ad = 0.004; (c) Ad = 0.008; (d) Ad = 0.016; (e) Ad = 0.032; (f) Ad = 0.064.

Thirdly, The adhesiveness parameter $\mathrm{Ad} = \gamma/(\rho_p U^2 d_p)$ is varied from 0.001 to 0.064 resulting in particles that behave only weakly adhesive to highly adhesive. Regardless of adhesiveness parameter, the particle concentration throughout the flow field is observed to be more or less uniform with a peak at the wall that increases with adhesiveness parameter due to particles adhering

to the wall.

Acknowledgement

The study is financially sponsored by The Danish Council for Strategic Research (No. 1305-00036B). Coupled CFD-DEM simulations were carried out on the Abacus 2.0 cluster located at the DeIC National HPC Centre, Southern University of Denmark (SDU).

References

[1] P. Saffman, J. Turner, On the collision of drops in turbulent clouds, Journal of Fluid Mechanics 1 (1956) 16–30, DOI: http://doi.org/10.1017/S0022112056000020.

[2] J. Abrahamson, Collision rates of small particles in a vigorously turbulent fluid, Chemical Engineering Science 30 (1975) 1371–1379, DOI: http://doi.org/10.1016/0009-2<509(75)85067-6.

[3] C. Meyer, D. Deglon, Particle collision modeling - A review, Minerals Engineering 24 (2011) 719–730, DOI: http://doi.org/10.1016/j.mineng.2011.03.015.

[4] B. K. Brunk, D. L. Kock, L. W. Lion, Turbulent coagulation of colloidal particles, Journal of Fluid Mechanics 364 (1998) 81–113, DOI: http://doi.org/10.1017/S0022112098001037.

[5] B. K. Brunk, D. L. Kock, L. W. Lion, Observations of coagulation in isotropic turbulence, Journal of Fluid Mechanics 371 (1998) 81–107, DOI: http://doi.org/10.1017/S0022112098001037.

[6] A. Brasil, T. Farias, M.G.Carvalho, U. Koylu, Numerical Characterization of the morphology of aggregated particles, Aerosol Science 32 (2001) 489–508, DOI: http://doi.org/10.1016/S0021-8502(00)00097-5.

[7] M. Sommerfeld, S. Stübing, A novel Lagrangian agglomerate structure model, Powder Technology 319 (2017) 34–52, DOI: http://dx.doi.org/10.1016/j.powtec.2017.06.016.

[8] J. Marshall, Particle aggregation and capture by walls in a particulate aerosol channel flow, Aerosol Science 38 (2007) 333–351, DOI: http://dx.doi.org/j.jaerosci.2007.01.004.

[9] T. Kobayashi, T. Tanaka, N. Shimada, T. Kawaguchi, DEM-CFD analysis of fluidization behavior of Geldart Group A particles using a dynamic adhesion force model, Powder Technology 248 (2013) 143–152, DOI: http://dx.doi.org/10.1016/j.powtec.2013.02.028.

[10] Y. Gu, A. Ozel, S. Sundaresan, A modified cohesion model for CFD-DEM simulations of fluidization, Powder Technology 296 (2016) 17–28, DOI: http://dx.doi.org/10.1016/j.powtec.2015.09.037.

[11] J. Hærvig, U. Kleinhans, C. Wieland, H. Spliethoff, A. L. Jensen, K. Sørensen, T. J. Condra, On the Adhesive JKR Contact and Rolling Models for Reduced Particle Stiffness Discrete Element Simulations, Powder Technology 319 (2017) 472–482, DOI: http://doi.org/10.1016/j.powtec.2017.07.006.

[12] F. D. Dizaji, J. S. Marshall, On the Significance of Two-Way Coupling in Simulation of Turbulent Particle Agglomeration, Powder Technology 318 (2017) 83–94, DOI: http://doi.org/10.1016/j.powtec.2017.05.027.

[13] S. Ergun, A. A. Orning, Fluid Flow through Randomly Packed Columns and Fluidized Beds, Industrial & Engineering Chemistry 41 (1949) 1179–1184, DOI: http://doi.org/10.1021/ie50474a011.

[14] R. J. Hill, D. L. Koch, A. J. Ladd, The first effects of fluid inertia on flows in ordered and random arrays of spheres, Journal of Fluid Mechanics 448 (2001) 213–241, DOI: http://dx.doi.org/10.1017/S0022112001005948.

[15] R. J. Hill, D. L. Koch, A. J. Ladd, Moderate-Reynolds-number flows in ordered and random arrays of spheres, Journal of Fluid Mechanics 448 (2001) 243–278, DOI: https://doi.org/10.1017/S0022112001005936.

[16] M. Dietzel, M. Sommerfeld, Numerical calculation of flow resistance for agglomerates with different morphology by the Lattice-Boltzmann Method, Powder Technology 250 (2013) 122–137, DOI: http://doi.org/10.1016/j.powtec.2013.09.023.

[17] M. Afkhami, A. Hassanpour, M. Fairweather, D. Njobuenwu, Fully coupled LES-DEM of particle interaction and agglomeration in a turbulent channel flow, Computers and Chemical Engineering 78 (2015) 24–38, DOI: http://dx.doi.org/10.1016/j.compchemeng.2015.04.003.

[18] F. Nicoud, F. Ducros, Subgrid-scale Stress Modelling Based on the Square of the Velocity Gradient Tensor, Flow, Turbulence and Combustion 62 (1999) 183–200, DOI: http://dx.doi.org/10.1023/A:1009995426001.

[19] P. Cundall, O. Strack, A discrete numerical model for granular assemblies, Géotechnique 29 (1979) 47–65, DOI: http://dx.doi.org/10.1680/geot.1979.29.1.47.

[20] K. L. Johnson, K. Kendall, A. D. Roberts, Surface energy and the contact of elastic solids, Proc. R. Soc. Lond. 324 (1971) 301–313, DOI: http://dx.doi.org/10.1098/rspa.1971.0141.

[21] D. Tabor, Surface Forces and Surface Interactions, Journal of Colloid and Interface Science 58 (1975) 2–13, DOI: http://dx.doi.org/10.1016/0021-9797(77)90366-6.

[22] J. N. Israelachvili, Intermolecular and Surface Forces, Academic Press, 2. edn., iSBN: 978-0-12-375182-9, 1992.

[23] E. J. R. Parteli, J. Schmidt, C. Brümel, K.-E. Wirth, W. Peukert, T. Pöschel, Attractive particle interaction forces and packing density

of fine glass powders, Nature Scientific Reports 4 (2014) 1–7, DOI: http://dx.doi.org/10.1038/srep06227.

[24] X. Deng, J. V. Scicolone, R. N. Davé, Discrete element method simulation of cohesive particles mixing under magnetically assisted impaction, Powder Technology 243 (2013) 96–109, DOI: http://dx.doi.org/10.1016/j.powtec.2013.03.043.

[25] C. Thornton, Interparticle sliding in the presence of adhesion, Journal of Physics D: Applied Physics 24 (1991) 1942–1946, DOI: http://doi.org/10.1088/0022-3727/24/11/007.

[26] C. Thornton, K. Yin, Impact of elastic spheres with and without adhesion, Powder Technology 65 (1991) 153–166, DOI: http://dx.doi.org/10.1016/0032-5910(91)80178-L.

[27] M. Oda, J. Konishi, S. Nemat-Nasser, Experimental micromechanical evaluation of strength of granular materials: Effects of particle rolling, Mechanics of Materials 1 (1982) 269–283, DOI: http://dx.doi.org/10.1016/0167-6636(82)90027-8.

[28] K. Iwashita, M. Oda, Rolling resistance at contacts in simulation of shear band development by DEM, Journal of Engineering Mechanics 124 (1998) 285–292, DOI: http://doi.org/10.1061/(ASCE)0733-9399(1998)124:3(285).

[29] C. Dominik, A. Tielens, Resistance to rolling in the adhesive contact of two elastic spheres, Philosophical Magazine A 72 (1995) 783–803, DOI: http://dx.doi.org/10.1080/01418619508243800.

[30] C. Dominik, A. Tielens, The Physics of Dust Coagulation and the Structure of Dust Aggregates in Space, The Astrophysical Journal 480 (1997) 647–673, DOI: http://dx.doi.org/10.1086/303996.

[31] S. Krijt, C. Dominik, A. Tielens, Rolling friction of adhesive microspheres, Journal of Physics D: Applied Physics 47 (2014) 175302 (9pp), DOI: http://dx.doi.org/10.1088/0022-3727/47/17/175302.

[32] P. Gondret, E. Hallouin, M. Lance, L. Petit, Experiments on the motion of a solid sphere toward a wall: From viscous dissipation to elastohydrodynamic bouncing, Physics of Fluids 11 (1999) 2803–2805, DOI: http://dx.doi.org/10.1063/1.870109.

[33] P. Gondret, M. Lance, L. Petit, Bouncing motion of spherical particles in fluids, Physics of Fluids 14 (2002) 643–652, DOI: http://dx.doi.org/10.1063/1.1427920.

[34] D. Legendre, C. Daniel, P. Guiraud, Experimental study of a drop bouncing on a wall in a liquid, Physics of Fluids 17 (2005) 097105, DOI: http://dx.doi.org/10.1063/1.2010527.

[35] C. Dritselis, Numerical study of particle deposition in a turbulent channel flow with transverse roughness elements on one wall, International Journal of Multiphase Flow 91 (2017) 1–18, DOI: http://dx.doi.org/10.1016/j.ijmultiphaseflow.2017.01.004.

[36] V. Armenio, V. Fiorotto, The importance of the forces acting on particles in turbulent flows, Physics of Fluids 13 (2001) 2437, DOI: http://dx.doi.org/10.1063/1.1385390.

[37] J. Marshall, Adhesive Particle Flow - A Discrete-Element Approach, Cambridge University Press, 1. edn., iSBN: 978-1-1-107-03207-1, 2014.

[38] S. Benyahia, M. Syamlal, T. J. O'Brien, Extension of Hill-Koch-Ladd drag correlation over all ranges of Reynolds number and solids volume fraction, Powder Technology 162 (2006) 166–174, DOI: http://dx.doi.org/10.1016/j.powtec.2005.12.014.

[39] J. B. McLaughlin, Aerosol particle deposition in numerically simulated channel flow, Physics of Fluids A 1 (1989) 1211, DOI: http://dx.doi.org/10.1063/1.857344.

[40] R. Kurose, S. Komori, Drag and lift forces on a rotating sphere in a linear shear flow, Journal of Fluid Mechanics 384 (1999) 183–206, DOI: http://doi.org/10.1017/S0022112099004164.

[41] J. B. McLaughlin, Inertial migration of a small sphere in linear shear flows, Journal of Fluid Mechanics 224 (1991) 261–274, DOI: http://doi.org/10.1017/S0022112091001751.

[42] S. K. Robinson, Coherent motions in the turbulent boundary layer, Annual Review of Fluid Mechanics 23 (1991) 601–639, DOI: http://dx.doi.org/10.1146/annurev.fl.23.010191.003125.

[43] J. den Toonder, F. Nieuwstadt, Reynolds number effects in a turbulent pipe flow for low to moderate Re, Physics of Fluids 9 (1997) 3398–3409, DOI: http://dx.doi.org/10.1063/1.869451.

[44] V. Armenio, Effect of the subgrid scales on particle motion, Physics of Fluids 11 (1999) 3030, DOI: http://dx.doi.org/10.1063/1.870162.

Nomenclature

$\mathrm{Ad} = \gamma/(\rho_\mathrm{p} U^2 d_\mathrm{p})$	Adhesiveness parameter	-
$\mathrm{Fr} = U/\sqrt{g_\mathrm{r} d_\mathrm{p}}$	Froude number	-
D	Pipe diameter	m
d_p	Particle diameter	m
$g_\mathrm{r} = (1 - 1/\chi)g$	Buoyancy corrected gravity	$\mathrm{m/s^2}$
$\mathrm{Kn} = \lambda/d_\mathrm{p}$	Knudsen number	-
L	Length of pipe section	m
p	Pressure	Pa
R	Effective particle radius	m
R	Pipe radius	m
r	Particle radius	m
r	Radial position	m
t	Time	s
$t^+ = tU/D$	Dimensionless time	-
U	Fluid bulk velocity	m/s
V	Cell volume	$\mathrm{m^3}$
$\mathrm{Re} = U\rho_\mathrm{f} D/\mu$	Reynolds number	-
$\mathrm{St} = \rho_\mathrm{p} d_\mathrm{p}^2 U/(18\mu D)$	Stokes number	-

Greek letters

δ	Kroneckers delta	-
δt	Time step size	s
Δ	Cell length	m
$\Delta\gamma/\gamma$	Adhesion hysteresis parameter	-
$\epsilon = d_\mathrm{p}/D$	Dimensionless particle diameter	-
$\lambda = E/(\rho_\mathrm{p} U^2)$	Elasticity parameter	-
λ	Mean free molecular path	m
μ	Dynamic viscosity	kg/(m·s)
ρ	Density	$\mathrm{kg/m^3}$
τ	Response time	s
$\chi = \rho_\mathrm{f}/\rho_\mathrm{p}$	Density ratio	-

Subscripts

f	Fluid
i,j	particle indices
mod	Stiffness-modified values
p	Particle
x, y, z	Spatial coordinates

Superscripts

$-$	Filtered values
$+$	Viscous units

Acronyms

sgs	Sub-grid scale
CFD	Computational Fluid Dynamics
DEM	Discrete Element Method
DNS	Direct Numerical Simulation
LES	Large Eddy Simulation
WALE	Wall-Adapting Local Eddy-viscosity